

Powell, J., Issler, D., Schneider, D., Fallas, K., and Stockli, D., 2019, Thermal history of the Mackenzie Plain, Northwest Territories, Canada: Insights from low-temperature thermochronology of the Devonian Imperial Formation: GSA Bulletin, <https://doi.org/10.1130/B35089.1>.

Data Repository

Contents:

- Expanded AHe, ZHe and AFT methods and results
- Expanded organic thermal maturity methods and results
- Comment on AFTINV software and AHe inverse modeling
- Figures S1–S12
- Tables S1–S7

Introduction

This supporting information incorporates text on analytical methods, expanded results figures that illustrate the apatite (U-Th)/He inverse thermal history models, and radial plots for all fission track samples. Additionally, it includes tables that show fission track age, track length distribution and chemistry for the four samples discussed in the manuscript, organic thermal maturity data used in thermal history modeling, and Cretaceous stratigraphic thicknesses used in AHe inverse history modeling.

Text S1. Analytical methods and results

Table S1. Summary of AFT age data, Imperial Formation, Mackenzie Plain, NWT, Canada

Table S2. Summary of AFT length data, Imperial Formation, Mackenzie Plain, NWT, Canada

Table S3. Apatite chemistry for all AFT age and length grains, Imperial Formation, Mackenzie Plain, NWT, Canada

Table S4. Organic thermal maturity for four Imperial Formation samples from the Mackenzie Plain, NWT, Canada

Table S5. Thermal history model inputs, data sources and assumptions

Table S6. Rock-Eval data for Devonian and Cretaceous outcrop samples proximal to 10FNA066, JP019, and well N-22, Mackenzie Plain, NWT, Canada

Table S7. Summary of Cretaceous stratigraphic age and thickness for the Mackenzie Plain, NWT, Canada

Text S1

1.1. APATITE AND ZIRCON (U-Th)/He METHOD

Apatite and zircon (U-Th)/He analyses were conducted at the University of Texas Geo-Thermochronometry Lab (Austin, USA), and follow common (U-Th)/He dating conventions (Wolfe and Stockli, 2010; Stockli et al., 2000). Following standard mineral separation, apatite and zircon were handpicked using a customized Nikon SMZ-U/100 stereomicroscope, and photographed using Nikon digital ColorView® camera. Grain dimensions were measured using the AnalySIS® software. In an effort to pick inclusion-free apatite, all grains analyzed were carefully screened for inclusions in isopropanol at 180x magnification. Apatite and zircon grains were wrapped in Pt foil and degassed using in-vacuo diode laser heating at 1050 °C and 1300 °C, respectively. ^4He was measured via quadrupole ultra-high vacuum noble gas extraction and mass-spectrometry system with a cryogenic trap. A ^3He spike was used for isotope dilution. All apatites were degassed twice to ensure complete degassing, and zircons were repeatedly heated until He yields were <1%. Degassed single grains were dissolved for ^{238}U , ^{232}Th , ^{149}Sm determinations by isotope dilution using an Element 2 ICP-MS. HNO_3 was used for apatite dissolution, whereas zircon were dissolved using a HF-HCl two-step pressure vessel procedure. All data were corrected for the effects of helium ejection (Farley et al., 1996). AHe and ZHe dates are reported with a standard error of 6% and 8%, respectively, which are reflective of the standard deviation of a population of analyzed standards.

Given that dispersion amongst AHe dates is common (Brown et al., 2013; Flowers et al., 2009; Murray et al., 2014), especially in rocks with protracted cooling histories (Fitzgerald et al., 2006; Ault et al., 2013) the 6% error applied to the AHe dates is likely not reflective of the true reproducibility of an analysis and may be too restrictive for modeling of the young AHe dates in this data set. Additionally, since many of these data were collected from 2012 through 2014, more recent grain-specific variables, including the effect of variable geometry (Brown et al., 2013; Beucher et al., 2013) and more recent methods for calculating Ft corrections (Ketcham et al., 2011) were not factored into data reduction. Nor were the dimensions in a second crystallographic width, as Ft corrections were generated under the assumption that the crystallographic A- and B-axes are equidimensional. This could be problematic, as most detrital apatite are beveled to some degree, and as a result the crystal volume and mass derived from the apatite geometry may be an overestimate.

Due to the above reasons, ages and eU concentrations used in modeling were recalculated from the original data to test the effect of broken crystals, varying grain morphologies, different methods for calculating the Ft correction and a B-axis that is 75% the diameter of the A-axis. The modeled date, error and eU concentrations are an average of the difference between our original corrected dates and the recalculated values. Overall, the modeled AHe date is <5% different than the original corrected date, and the errors used in modeling are ~10% the modeled date. Modeled eU concentrations are mostly within 5% of the original values, but can be substantially larger when the mass of the recalculated grain is substantially less than the original value. This is especially evident in grain JPCPC4–5, where the mass of the bipyramidal grain with a smaller second width is much less than initially calculated (1.05 μg vs 1.89 μg). Whereas these modeled ages do not represent a “truer” AHe date than those reported, they are perhaps a better representation of plausible variability in detrital AHe dates than the standard 6% error.

A suite of 53 single-grain AHe dates was collected from the six Imperial Formation samples. Sixteen ZHe dates were acquired from three Imperial Formation samples in which zircon grains were present (**Table 2**). Sample JPCPC3 has seven AHe dates that range from 37.0 ± 2.2 – 55.3 ± 3.3 Ma and four ZHe dates that form two disparate populations younger than the depositional age (39.9 ± 3.2 – 49.7 ± 4.0 Ma; 271.9 ± 21.8 – 300.7 ± 24.1 Ma). The eU concentrations for apatite and zircon grains lie between 33 and 79 ppm and 21–611 ppm, respectively. Ten apatite grains from sample JPCPC4 yield AHe dates between 38.2 ± 2.3 – 132.9 ± 8.0 Ma. AHe dates have no obvious trend with respect to eU concentration, which varies from 18 to 40 ppm in the sample. Ten apatite and six zircon (U-Th)/He dates were acquired from the Imperial anticline sample 10FNA066. AHe dates range from 3.2 ± 0.2 – 47.7 ± 2.9 Ma and are positively correlated with increasing eU concentration (1–119 ppm). ZHe dates span 169.9 ± 13.6 – 390.4 ± 31.2 Ma over an eU range of 66–239 ppm. Sample JP019 from Norman Wells had few apatite grains and only yielded five AHe dates. Four of these dates are between 17.0 ± 1.0 and 37.2 ± 2.2 Ma, with the fifth grain yielding a much older 224.9 ± 13.5 Ma. This large range in AHe dates does not correspond with increases in the eU concentration from 14 to 50 ppm. The ten AHe dates from sample 10FNARL008 are positively correlated with eU concentration, increasing gradually from 15.0 ± 0.9 – 47.9 ± 2.9 Ma as eU increases 25–125 ppm. The furthest southeast sample, Husky7, has eleven AHe dates that range from 12.7 ± 1.0 – 67.2 ± 5.4 Ma. Dispersion within the sample cannot be explained with respect to increasing eU concentrations (21–94 ppm). Six ZHe dates from the adjacent sample, Husky6, are broadly scattered from 96.7 ± 7.7 – 414.7 ± 33.2 Ma. With the exception of a single data point, the ZHe dates are negatively correlated with eU concentration.

1.2 LA-ICP-MS Fission Track Method

The four samples processed for apatite fission track thermochronology were analyzed using the laser ablation inductively coupled plasma mass spectrometry method (LA-ICP-MS) method (Donelick et al., 2005; Chew and Donelick, 2012; Hasebe et al., 2004) and the modified zeta calibration (Hurford and Green, 1983; Hasebe et al., 2004). Samples were analyzed by Paul O’Sullivan at Apatite to Zircon, Incorporated (Viola, USA) using a Resonetics M-50 193 nm ArF excimer laser-ablation system coupled to an Agilent 7700x quadrupole ICP-MS. Laser ablation was conducted using a 26 μm spot and a 7 Hz laser repetition rate with the laser set in constant energy mode. Fission tracks were viewed and counted or measured at 2000x (Zeiss Axioplan microscope) dry magnification using unpolarized, transmitted light with or without reflected light. All AFT age (**Table S1**) and length grains (**Table S2**) were selected to sample the greatest range of observable characteristics (size, degree of roundness, color, etch figure size, etc.). Durango (DR) was used as the apatite FT zeta age calibration standard. During each LA-ICP-MS session containing samples of unknown FT age, clusters of ~ 10 zeta spots were analyzed during the session for purposes of calibrating $^{238}\text{U}/^{43}\text{Ca}$. Ratios of primary zeta (original zeta LA-ICP-MS session) to secondary zeta (current LA-ICP-MS session) $^{238}\text{U}/^{43}\text{Ca}$ were determined for each zeta calibration spot and smoothed using a load-specific running-median method. Only spots visited during the primary, original zeta LA-ICP-MS session were revisited during the secondary, current LA-ICP-MS session for this purpose. This method is analogous to using ^{235}U -doped glass standards in the external detector method of fission track analysis (Donelick et al., 2005); in this study, specific DR grains from the primary standard LA-ICP-MS session serve as ^{235}U -doped standards.

In an effort to understand the uranium content and range of chemistry present in our sample suite, all grains analyzed for AFTA were measured for major, minor and REE geochemistry. Analyses were conducted via LA-ICP-MS methods at Apatite to Zircon, Inc. (Viola, USA) using a Resonetics M-50-LR 193 nm ArF Excimer laser ablation system coupled to an Agilent 7700x quadrupole inductively coupled mass spectrometer (ICP-MS). The laser was operated at a repetition rate of 10 Hz, with a lateral spot size of 10 μm , and pulse energy of 0.422 mJ. In addition to the LA-ICP-MS data, major elements and halogens were analyzed at the University of Ottawa (Ottawa, Canada) to recalculate $r_{\text{mr}0}$ values for samples that exhibited substantial kinetic overlap using $r_{\text{mr}0}$ values from LA-ICP-MS derived chemistry. EPMA chemistry was measured using the JEOL JXA-8230 SuperProbe at the University of Ottawa, which was operated with an accelerating voltage of 10 kV and beam current of 3.8 nA to focus and concentrate the electron beam to a minimum of 1 μm . These conditions were employed to better determine the halogen content in JPCPC3, and JPCPC4 and in particular, to assess the effect of hydroxyl on calculated $r_{\text{mr}0}$ values. Additionally, Husky7, Husky6 and JP019 were analyzed using the microprobe at Washington State University (Pullman, USA). We use the stoichiometric relationships (Ketcham, 2015) to convert measured weight% oxide values to atoms per formula unit (apfu), and later use these values to calculate grain-specific $r_{\text{mr}0}$ values (**Table S3**). We opt to use the original $r_{\text{mr}0}$ calculation (Carlson et al., 1999) over the more recent derivation (Ketcham et al., 2007), as the newer equation is based on combined annealing experiments from different labs, which may introduce systematic error to the calculated values.

Of the seven samples analyzed for (U-Th)/He analysis, six yielded sufficient apatite for apatite fission track analysis. Each sample exhibits substantial dispersion in AFT dates, and fails the χ^2 test, indicating that the data do not comprise single kinetic populations. We use the kinetic parameter $r_{\text{mr}0}$ (Ketcham et al., 1999) to isolate statistically significant AFT populations and report their pooled age and mean track length (**Table 1**). Twenty-eight AFT dates for sample JPCPC3 span 22.0 ± 22.1 – 220.3 ± 79.1 Ma. Two kinetic populations were identified on the basis of their $r_{\text{mr}0}$ values (50.2 ± 2.9 Ma, 13.6 ± 1.8 μm ; 170.1 ± 24.7 Ma, 14.1 ± 2.2 μm). Sample JPCPC4 has thirty-four AFT dates that range from 23.1 ± 16.4 – 484.9 ± 118.4 Ma. These dates were separated into three statistically significant populations (45.7 ± 4.1 Ma, 13.9 ± 1.5 μm ; 85.9 ± 6.9 Ma, 13.3 ± 2.1 μm ; 224.1 ± 14.5 Ma, 13.0 ± 2.4 μm). Sample 10FNARL008 yielded 26 AFT dates between 314.6 ± 63.6 and 9.2 ± 6.5 Ma and three discrete kinetic populations (11.2 ± 6.5 Ma, 11.4 ± 0.9 μm ; 46.0 ± 3.1 Ma, 13.6 ± 1.4 μm ; 225.4 ± 31.0 Ma, 12.2 ± 1.6 μm). The 23 AFT dates in Husky6 span 396.4 ± 64.0 and 42.0 ± 19.6 Ma, and are separated into two populations (71.1 ± 9.7 Ma, 12.3 ± 2.1 μm ; 125.2 ± 12.2 , 13.0 ± 1.5 μm). A third population (342.3 ± 45.1 Ma) is poorly defined in $r_{\text{mr}0}$ space and is not assigned any track lengths. Finally, the 33 AFT dates from sample Husky7 are between 353.94 ± 166.6 and 14.6 ± 14.8 Ma. These AFT data were separated into three distinct kinetic populations on the basis of their date and $r_{\text{mr}0}$ values (40.6 ± 4.8 Ma, 13.5 ± 1.2 μm ; 97.3 ± 9.3 Ma, 12.1 ± 2.4 μm ; 240.7 ± 21.5 Ma, 12.5 ± 2.0 μm).

Sample JP019 was processed as two aliquots. The first aliquot (DIF-1) was analyzed in 2012 by A to Z Inc. using the AFT LA-ICPMS method. Also, apatite elemental data were acquired using the LA-ICPMS method to help constrain multi-kinetic interpretations. The sample has significant AFT age dispersion and fails the χ^2 -test for assessing whether the data can be described by a single age component. At the time, it was uncertain how to interpret the sample because there was no clear relationship between AFT age and the kinetic parameters, $r_{\text{mr}0}$ and D_{par} . As a result, it was not possible to determine the relative importance of annealing kinetic

effects and variable apatite provenance in controlling the sample AFT age dispersion. Subsequently it was realized that OH content is an important parameter for calculating r_{mr0} values. Therefore a second aliquot of the sample (159–08) was analyzed in 2017 by GeoSep using the AFT LA-ICPMS method and apatite elemental data were acquired using electron probe microanalysis at Washington State University. The new data show less AFT age scatter and better resolution of AFT kinetic populations with respect to the r_{mr0} parameter. The two data sets were combined in such a way that the same modified zeta value could be used for both data sets to calculate AFT ages. This was achieved by multiplying the $^{238}\text{U}/^{43}\text{Ca}$ ratio for each age grain in aliquot 1 by the ratio of aliquot 2 modified zeta over aliquot 1 modified zeta. The modified zeta value for aliquot 2 yields the same original AFT ages for aliquot 1 grains when the modified ratios are substituted into the AFT age equation.

The combined AFT data are interpreted as having three statistical AFT kinetic populations based on plots of AFT age and length with respect to the r_{mr0} parameter (converted to effective Cl using elemental data). Age mixture modeling (DensityPlotter) yields three AFT populations with similar ages to the kinetic populations inferred from the elemental data. The kinetic parameter plots show overlap of age and length grains between different AFT populations but much of this overlap is because of systematic differences in r_{mr0} values between aliquots 1 and 2. The absence of OH values for aliquot 1 grains increases r_{mr0} values, making the grains appear to be less track retentive compared with those for aliquot 2. Both aliquots were interpreted separately and then combined together in composite plots. Grain location information (to identify grains having both age and length data) and Dpar values were used to help sort data for grains that lack elemental data. Kinetic population 2 has the best determined annealing kinetic parameter because its apatite grains have compositions that are similar to the typical F-apatite used for the annealing experiments on which the kinetic model is based. The mid-point of the range of effective Cl values was used to define the representative effective Cl value for kinetic population 2. This is preferred over using the average effective Cl value because of the systematic differences in r_{mr0} values for aliquots 1 and 2. Kinetic parameters for the other two populations were determined through thermal modeling. Kinetic population 1 is inferred to have very low retentivity and this has been observed for other imperial Formation samples. Kinetic population 3 is required to have extremely high retentivity (similar to Bamble, Norway apatite) in order for the model to fit AFT parameters for all three populations.

Comparatively, **Figures S1 - S5** show radial plots (Vermeesch, 2009) for all four fission track samples. These plots graphically compare AFT dates with different precisions and can identify different AFT date populations within a single sample. Overall, there is good agreement between AFT kinetic populations recognized on the basis of r_{mr0} and those identified graphically.

1.3. Vitrinite Reflectance and Rock Eval

Vitrinite reflectance and Rock-Eval pyrolysis analyses were undertaken at the Geological Survey of Canada (Calgary, Canada). A short discussion on the techniques is included below, but is expanded upon in many GSC open file reports (Issler et al., 2012, 2016).

Vitrinite reflectance is based on the percentage of incident light reflected from polished vitrinite macerals and is commonly used in sedimentary basin thermal history analysis. Kinetic models that account for the increase of vitrinite reflectance values with increasing burial temperature include the EASY%Ro calibration (Sweeney and Burnham, 1990) and the basin%Ro calibration (Nielsen et al., 2017). Crushed rock material between 1 and 10 mm in size

is mounted into epoxy, ground using carborundum and diamond grit, and polished using a cloth and an alumina-water slurry. Microscopes used for study include a Zeiss UMSP microscope fitted with a UMP photometer and a Leitz MPM II with a PC-controller system. Organic material was observed under magnification (up to 2000x) with white and fluorescent light sources and oil, air and water immersion objectives. %Ro values were measured for several organic macerals and compared with glass standards of known refractive indices.

Rock-Eval pyrolysis was conducted on four samples using the Rock-Eval 6 machine at the GSC Calgary office. Rock-Eval pyrolysis is a technique that assesses the abundance, quality and thermal maturity of organic matter in sedimentary rocks. In this method, rock material is crushed into a powder, separated into ~70 mg aliquots and placed into stainless steel crucibles. Samples undergo non-isothermal pyrolysis in an inert atmosphere (nitrogen) to yield hydrocarbons (S1 and S2 curves) and oxidized carbon from organics and mineral sources (S3). Following the pyrolysis, samples are heated in an oxidation oven to determine the weight percent of total organic carbon (TOC).

Samples JPCPC3, JPCPC4, 10FNA066 and 10FNARL008 were organically-lean sandstones and were analyzed for both organic thermal maturity and Rock-Eval pyrolysis (**Table S4**). Organic petrology measured the reflectance of bitumen, vitrinite and recycled vitrinite. Due to the low number of measurements of natural vitrinite, the thermal maturity indicated from these reflectance data should be considered as broad estimates. Likewise, %Ro equivalents from bitumen reflectance may be measuring migrated bitumen, and as a result reflects the lower boundary of the true maturity. Thermal maturity as indicated by Rock-Eval pyrolysis Tmax data from the same samples are in many cases spurious due to the low weight % TOC values and S2 values. **Table S6** is comprised of pertinent Rock-Eval data for Cretaceous and Devonian outcrop samples proximal to 10FNA066, JP019 and well N-22.

In manuscript Figure 10, Rock-Eval pyrolysis data from wells in the Mackenzie Plain (Feinstein et al., 1988) were deemed suspect if total organic carbon was <0.5 wt% or if the value corresponding to the S2 curve was <0.5 mg HC/g of initial rock (Issler et al., 2012, 2016), and egregious data were not converted to %Ro equivalents. The depth of stratigraphic formation tops were taken from publically available databases (NEB, 2013; Hadlari et al., 2013) and used to determine stratigraphic ages and thicknesses (**Table S7**). Present day geothermal gradients were calculated from borehole logging and drillstem test data (Majorowicz and Morrow, 1998; Geotech, 1984) assuming a surface temperature of 0 °C due to regional permafrost.

1.4. AFTINV Thermal History Modeling Software

AFTINV(Issler, 1996) (Issler, 1996; Issler et al., 2005) is an AFT inverse model that extracts thermal history information from multi-kinetic AFT data. AFTINV uses a non-directed Monte Carlo method to search parameter space for a user-specified set of (typically 300) unique thermal histories that 1) provide a statistical fit between modeled and observed track length distribution using the Kolmogorov-Smirnov (KS) statistic, and 2) have calculated AFT dates within two standard deviations of the measured data. Additionally, the program has been upgraded to incorporate multi-kinetic annealing equations (Ketcham et al., 1999, 2007) and the basin%Ro kinetic vitrinite reflectance model (Nielsen et al., 2017).

In addition to inverse modeling of AFT data, we performed inverse thermal history modeling of AHe data using HeFTy (Ketcham, 2005; version 1.9.1). Each inverse history model has specified time-temperature constraints through which the generated time-temperature paths

must pass. These constraints are defined using independent geologic information from preserved Cretaceous and Paleocene stratigraphy and known unconformities across the region (Hadlari et al., 2013; Yorath and Cook, 1981; Thomson et al., 2011; Dixon, 1999), and thermal history information from AFT modeling (**Figure 5, 6**). Two to three grains were chosen for modeling from each sample. These grains were selected to capture the realm of AHe date, eU and grain size variations within a given sample. Since the chemistry of each apatite is unknown, radiation damage annealing was modeled assuming a standard fluorapatite composition and r_{mr0} value of 0.83. Organic thermal maturity data for each sample were incorporated into modeling to constrain maximum temperatures (**Fig. S6 – S12**).

We follow the suggested thermochronology modeling reporting protocol of Flowers et al. (2015) and report all information on data inputs, data sources and modeling assumptions in **Table S5**. This data table details which samples are incorporated into inverse and forward models, and where the relevant data to reproduce those results can be retrieved.

REFERENCES CITED

- Ault, A.K., Flowers, R.M., and Bowring, S.A., 2013, Phanerozoic surface history of the Slave craton: *Tectonics*, v. 32, p. 1066–1083, <https://doi.org/10.1002/tect.20069>.
- Beucher, R., Brown, R.W., Roper, S., Stuart, F., and Persano, C., 2013, Natural age dispersion arising from the analysis of broken crystals. Part II: Practical application to apatite (U-Th)/He thermochronometry: *Geochimica et Cosmochimica Acta*, v. 120, p. 395–416, <https://doi.org/10.1016/j.gca.2013.05.042>.
- Brown, R.W., Beucher, R., Roper, S., Persano, C., Stuart, F., and Fitzgerald, P., 2013, Natural age dispersion arising from the analysis of broken crystals. Part I: Theoretical basis and implications for the apatite (U-Th)/He thermochronometer: *Geochimica et Cosmochimica Acta*, v. 122, p. 478–497, <https://doi.org/10.1016/j.gca.2013.05.041>.
- Carlson, W.D., Donelick, R.A., and Ketcham, R.A., 1999, Variability of apatite fission-track annealing kinetics: I. Experimental results: *The American Mineralogist*, v. 84, p. 1213–1223, <https://doi.org/10.2138/am-1999-0901>.
- Chew, D.M., and Donelick, R.A., 2012, Combined apatite fission track and U-Pb dating by LA-ICP-MS and its application in apatite provenance analysis: *Mineralogical Association of Canada Short Course*, v. 42, p. 219–247.
- Dixon, J., 1999, Mesozoic-Cenozoic stratigraphy of the northern Interior Plains and Plateaux, Northwest Territories: *Geological Survey of Canada Bulletin*, v. 536, p. 56, <https://doi.org/10.4095/210800>.
- Donelick, R.A., O’Sullivan, P.B., and Ketcham, R.A., 2005, Apatite Fission-Track Analysis: *Reviews in Mineralogy and Geochemistry*, v. 58, p. 49–94, <https://doi.org/10.2138/rmg.2005.58.3>.
- Farley, K.A., Wolf, R.A., and Silver, L.T., 1996, The effects of long alpha-stopping distances on (U-Th)/He ages: *Geochimica et Cosmochimica Acta*, v. 60, p. 4223–4229, [https://doi.org/10.1016/S0016-7037\(96\)00193-7](https://doi.org/10.1016/S0016-7037(96)00193-7).
- Feinstein, S., Brooks, P.W., Gentzis, T., Goodarzi, F., Snowdon, L.R., and Williams, G.K., 1988, Thermal maturity in the Mackenzie Corridor, Northwest and Yukon Territories, Canada: *Geological Survey of Canada, Open File 1944*, p. 65, <https://doi.org/10.4095/130457>.
- Feinstein, S., Williams, G.K., Snowdon, L.R., Goodarzi, F., and Gentzis, T., 1991b, Thermal maturation of organic matter in the Middle Devonian to Tertiary section, Fort Norman area

- (central Mackenzie Plain): *Canadian Journal of Earth Sciences*, v. 28, p. 1009–1018, <https://doi.org/10.1139/e91-092>.
- Feinstein, S., Issler, D.R., Snowdon, L.R., and Williams, G.K., 1996, Characterization of major unconformities by paleothermometric and paleobarometric methods: application to the Mackenzie Plain, Northwest Territories, Canada: *Bulletin of Canadian Petroleum Geology*, v. 44, p. 55–71.
- Fitzgerald, P.G., Baldwin, S.L., Webb, L.E., and O’Sullivan, P., 2006, Interpretation of (U–Th)/He single grain ages from slowly cooled crustal terranes: A case study from the Transantarctic Mountains of southern Victoria Land: *Chemical Geology*, v. 225, p. 91–120, <https://doi.org/10.1016/j.chemgeo.2005.09.001>.
- Flowers, R.M., Ketcham, R.A., Shuster, D.L., and Farley, K.A., 2009, Apatite (U–Th)/He thermochronometry using a radiation damage accumulation and annealing model: *Geochimica et Cosmochimica Acta*, v. 73, p. 2347–2365, <https://doi.org/10.1016/j.gca.2009.01.015>.
- Flowers, R.M., Farley, K.A., and Ketcham, R.A., 2015, A reporting protocol for thermochronologic modeling illustrated with data from the Grand Canyon: *Earth and Planetary Science Letters*, v. 432, p. 425–435, <https://doi.org/10.1016/j.epsl.2015.09.053>.
- Geotech, 1984, Subsurface Temperature Data from Wells North of Sixty Yukon—Northwest Territories.
- Guenther, W.R., Reiners, P.W., Ketcham, R.A., Nasdala, L., and Giester, G., 2013, Helium diffusion in natural zircon: Radiation damage, anisotropy, and the interpretation of zircon (U–Th)/He thermochronology: *American Journal of Science*, v. 313, p. 145–198, <https://doi.org/10.2475/03.2013.01>.
- Hadlari, T., MacLean, B.C., Galloway, J.M., Sweet, A.R., White, J.M., Thomson, D., Gabites, J., and Schröder-Adams, C.J., 2014, The flexural margin, the foredeep, and the orogenic margin of a northern Cordilleran foreland basin: Cretaceous tectonostratigraphy and detrital zircon provenance, northwestern Canada: *Marine and Petroleum Geology*, v. 57, p. 173–186, <https://doi.org/10.1016/j.marpetgeo.2014.05.019>.
- Hadlari, T., Midwinter, D., MacLean, B.C., Fallas, K.M., and Dixon, J., 2013, Formation tops and isopach maps of Cretaceous strata of Mackenzie Plain and parts of Peel Plain, Northwest Territories: Geological Survey of Canada, Open File 7326, p. 4, <https://doi.org/10.4095/293112>.
- Hasebe, N., Barbarand, J., Jarvis, K., Carter, A., and Hurford, A.J., 2004, Apatite fission-track chronometry using laser ablation ICP-MS: *Chemical Geology*, v. 207, p. 135–145, <https://doi.org/10.1016/j.chemgeo.2004.01.007>.
- Hurford, A.J., and Green, P.F., 1983, The zeta age calibration of fission-track dating: *Chemical Geology*, v. 41, p. 285–317, [https://doi.org/10.1016/S0009-2541\(83\)80026-6](https://doi.org/10.1016/S0009-2541(83)80026-6).
- Issler, D.R., 1996, An inverse model for extracting thermal histories from apatite fission track data: instructions and software for the Windows 95 environment: Geological Survey of Canada, Open File 2325, p. 85.
- Issler, D.R., Grist, A., and Stasiuk, L., 2005, Post-Early Devonian thermal constraints on hydrocarbon source rock maturation in the Keele Tectonic Zone, Tulita area, NWT, Canada, from multi-kinetic apatite fission track thermochronology, vitrinite reflectance and shale compaction: *Bulletin of Canadian Petroleum Geology*, v. 53, p. 405–431, <https://doi.org/10.2113/53.4.405>.

- Issler, D.R., Jiang, C., Reyes, J., and Obermajer, M., 2016, Integrated analysis of vitrinite reflectance, Rock-Eval 6, gas chromatography, and gas chromatography-mass spectrometry data for the Reindeer D-27 and Tununuk K-10 wells, Beaufort-Mackenzie Basin, northern Canada: Geological Survey of Canada, Open File 8047, p. 94, <https://doi.org/10.4095/297905>.
- Issler, D.R., Obermajer, M., Reyes, J., and Li, M., 2012, Integrated analysis of vitrinite reflectance, Rock-Eval 6, gas chromatography, and gas chromatography-mass spectrometry data for the Mallik A-06, Parsons N-10 and Kugaluk N-02 wells, Beaufort-Mackenzie Basin, northern Canada: Geological Survey of Canada, Open File 6978, p. 78, <https://doi.org/10.4095/289672>.
- Jarvie, D.M., Claxton, B.L., Henk, F., and Breyer, J.T., 2001, Oil and shale gas from the Barnett Shale, Fort Worth basin, Texas: AAPG National Convention, June 3–6, 2001, Denver, CO: AAPG Bulletin, v. 85, p. A100.
- Jiang, C., Pyle, L.J., and Gal, L.P., 2014, Organic geochemistry of petroleum hydrocarbons in Middle to Upper Devonian outcrop samples from Mackenzie Plain area: Northwest Territories Geoscience Office, NWT Open Report 2014-05.
- Ketcham, R.A., 2005, Forward and Inverse Modeling of Low-Temperature Thermochronometry Data: Reviews in Mineralogy and Geochemistry, v. 58, p. 275–314, <https://doi.org/10.2138/rmg.2005.58.11>.
- Ketcham, R.A., 2015, Technical Note: Calculation of stoichiometry from EMP data for apatite and other phases with mixing on monovalent anion sites: The American Mineralogist, v. 100, p. 1620–1623, <https://doi.org/10.2138/am-2015-5171>.
- Ketcham, R.A., Carter, A., Donelick, R.A., Barbarand, J., and Hurford, A.J., 2007, Improved modeling of fission-track annealing in apatite: The American Mineralogist, v. 92, p. 799–810, <https://doi.org/10.2138/am.2007.2281>.
- Ketcham, R.A., Donelick, R.A., and Carlson, W.D., 1999, Variability of apatite fission-track annealing kinetics: III. Extrapolation to geological time scales: The American Mineralogist, v. 84, p. 1235–1255, <https://doi.org/10.2138/am-1999-0903>.
- Ketcham, R.A., Gautheron, C., and Tassan-Got, L., 2011, Accounting for long alpha-particle stopping distances in (U-Th-Sm)/He geochronology: Refinement of the baseline case: Geochimica et Cosmochimica Acta, v. 75, p. 7779–7791, <https://doi.org/10.1016/j.gca.2011.10.011>.
- Majorowicz, J.A., and Morrow, D.W., 1998, Subsurface temperature and heat flow - Yukon and Northwest Territories: Geological Survey of Canada, Open File 3626, p. 6, <https://doi.org/10.4095/209923>.
- Murray, K.E., Orme, D.A., and Reiners, P.W., 2014, Effects of U-Th-rich grain boundary phases on apatite helium ages: Chemical Geology, v. 390, p. 135–151, <https://doi.org/10.1016/j.chemgeo.2014.09.023>.
- NEB, 2013, Table of Formation Tops: <https://www.neb-one.gc.ca/nrth/pblctn/tbfrmtntp-eng.html> (accessed September 2015).
- Nielsen, S.B., Clausen, O.R., and McGregor, E., 2017, Basin%Ro: A vitrinite reflectance model derived from basin and laboratory data: Basin Research, v. 29, p. 515–536, <https://doi.org/10.1111/bre.12160>.
- Powell, J., and Schneider, D.A., 2013, Preliminary results of $^{40}\text{Ar}/^{39}\text{Ar}$ geochronology from the eastern Mackenzie Mountains and Mackenzie Plain, Northwest Territories: Geological Survey of Canada Current Research, v. 2013-18, p. 16, <https://doi.org/10.4095/292712>.

- Powell, J., Schneider, D., Stockli, D., and Fallas, K., 2016, Zircon (U-Th)/He thermochronology of Neoproterozoic strata from the Mackenzie Mountains, Canada: Implications for the Phanerozoic exhumation and deformation history of the northern Canadian Cordillera: *Tectonics*, v. 35, p. 663–689, <https://doi.org/10.1002/2015TC003989>.
- Pyle, L.J., and Gal, L.P., 2014, Analytical Results from Cretaceous and Devonian Studies in Mackenzie Plain: Northwest Territories Geoscience Office, NWT Open Report 2014-006, p. 1–28.
- Snowdon, L.R., 1990, Rock-Eval/TOC data for 55 Northwest and Yukon Territories wells [60°–69°N]: Geological Survey of Canada, Open File 2327, p. 164, 10.4095/131489.
- Stockli, D.F., Farley, K.A., and Dumitru, T.A., 2000, Calibration of the apatite (U-Th)/He thermochronometer on an exhumed fault block, White Mountains, California: *Geology*, v. 28, p. 983–986, [https://doi.org/10.1130/0091-7613\(2000\)28<983:COTAHT>2.0.CO;2](https://doi.org/10.1130/0091-7613(2000)28<983:COTAHT>2.0.CO;2).
- Sweeney, J.J., and Burnham, A.K., 1990, Evaluation of a simple model of vitrinite reflectance based on chemical kinetics: *The American Association of Petroleum Geologists Bulletin*, v. 74, p. 1559–1570.
- Thomson, D., Schröder-Adams, C.J., Hadlari, T., Dix, G., and Davis, W.J., 2011, Albian to Turonian stratigraphy and palaeoenvironmental history of the northern Western Interior Sea in the Peel Plateau Region, Northwest Territories, Canada: *Palaeogeography, Palaeoclimatology, Palaeoecology*, v. 302, p. 270–300, <https://doi.org/10.1016/j.palaeo.2011.01.017>.
- Vermeesch, P., 2009, RadialPlotter: A Java application for fission track, luminescence and other radial plots: *Radiation Measurements*, v. 44, p. 409–410, <https://doi.org/10.1016/j.radmeas.2009.05.003>.
- Wolfe, M.R., and Stockli, D.F., 2010, Zircon (U-Th)/He thermochronometry in the KTB drill hole, Germany, and its implications for bulk He diffusion kinetics in zircon: *Earth and Planetary Science Letters*, v. 295, p. 69–82, <https://doi.org/10.1016/j.epsl.2010.03.025>.
- Yorath, C.J., and Cook, D.G., 1981, Cretaceous and Tertiary Stratigraphy and Paleogeography, Northern Interior Plains, District of Mackenzie: Geological Survey of Canada, Memoir, v. 398, p. 1–76, <https://doi.org/10.4095/109299>.

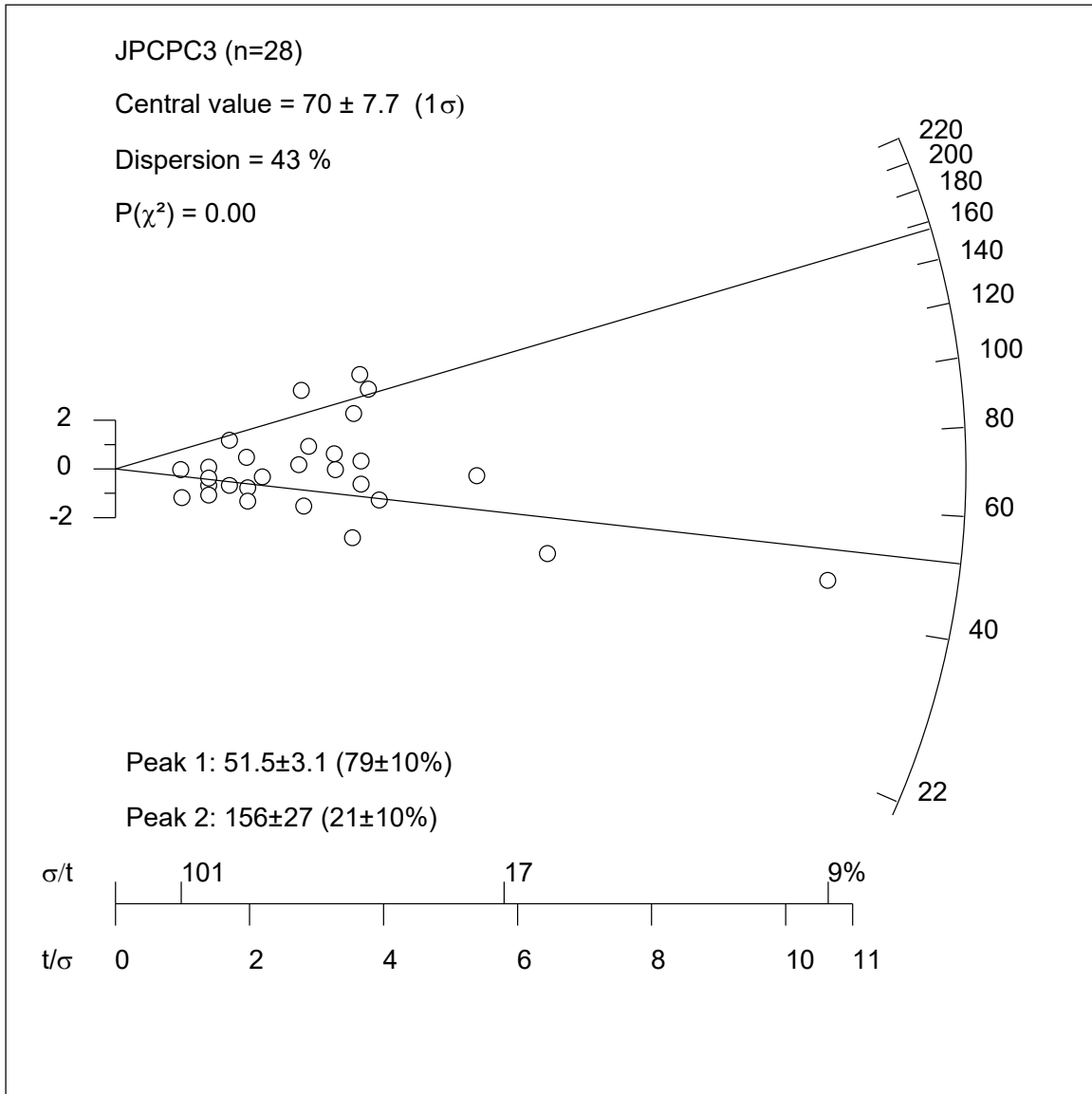


Fig. S1. Radial plot of the apatite fission track data for JPCPC3 using RadialPlotter (Vermeesch, 2009). Fission track dates and their associated error are plotted as a function of the degree of rotation along, and distance from, the curved axis. Pooled ages from proposed kinetic populations (Table 1, S1) are within error of the peak ages predicted from the radial plot.

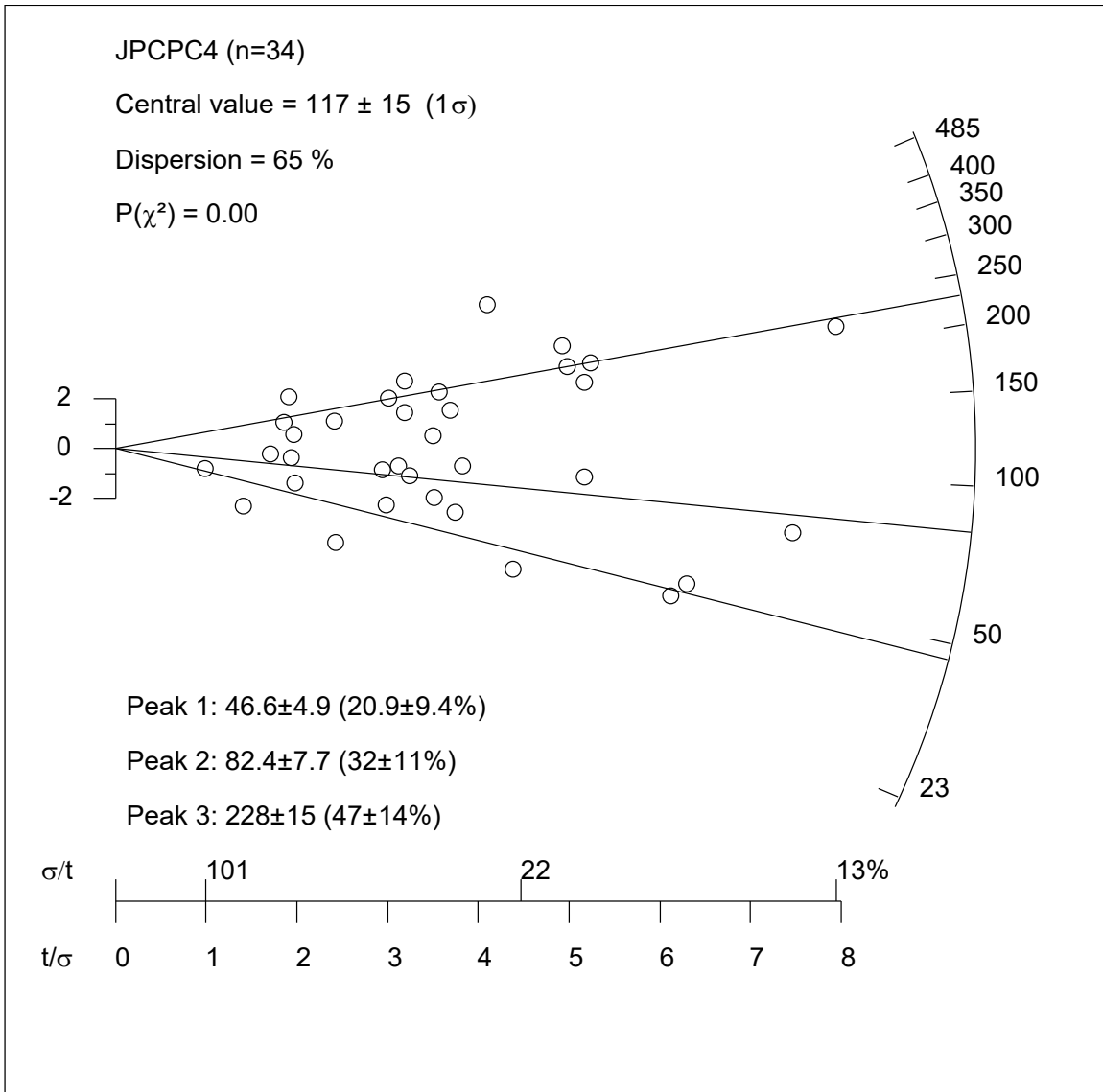


Fig. S2. Radial plot of the apatite fission track data for JPCPC4 using RadialPlotter (Vermeesch, 2009). Fission track dates and their associated error are plotted as a function of the degree of rotation along, and distance from, the curved axis. Pooled ages from proposed kinetic populations (Table 1, S1) are within error of the peak ages predicted from the radial plot.

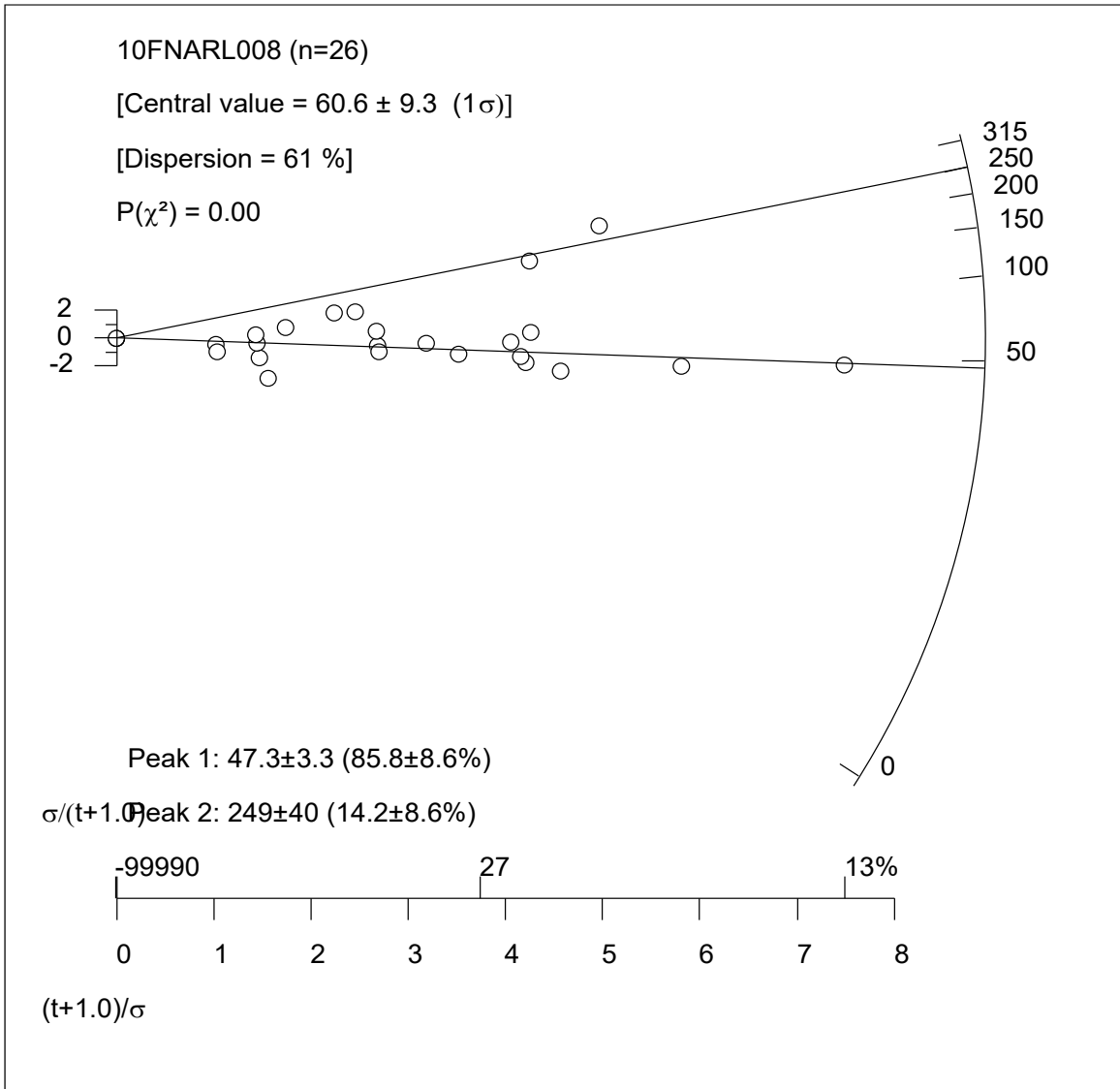


Fig. S3. Radial plot of the apatite fission track data for 10FNARL008 using RadialPlotter (Vermeesch, 2009). Fission track dates and their associated error are plotted as a function of the degree of rotation along, and distance from, the curved axis. Pooled ages from two of the three proposed kinetic populations (Table 1, S1) are within error of the peak ages predicted from the radial plot. However, the radial plot is not able to identify the third population recognized based on r_{mr0} values (11.2 ± 6.5 Ma).

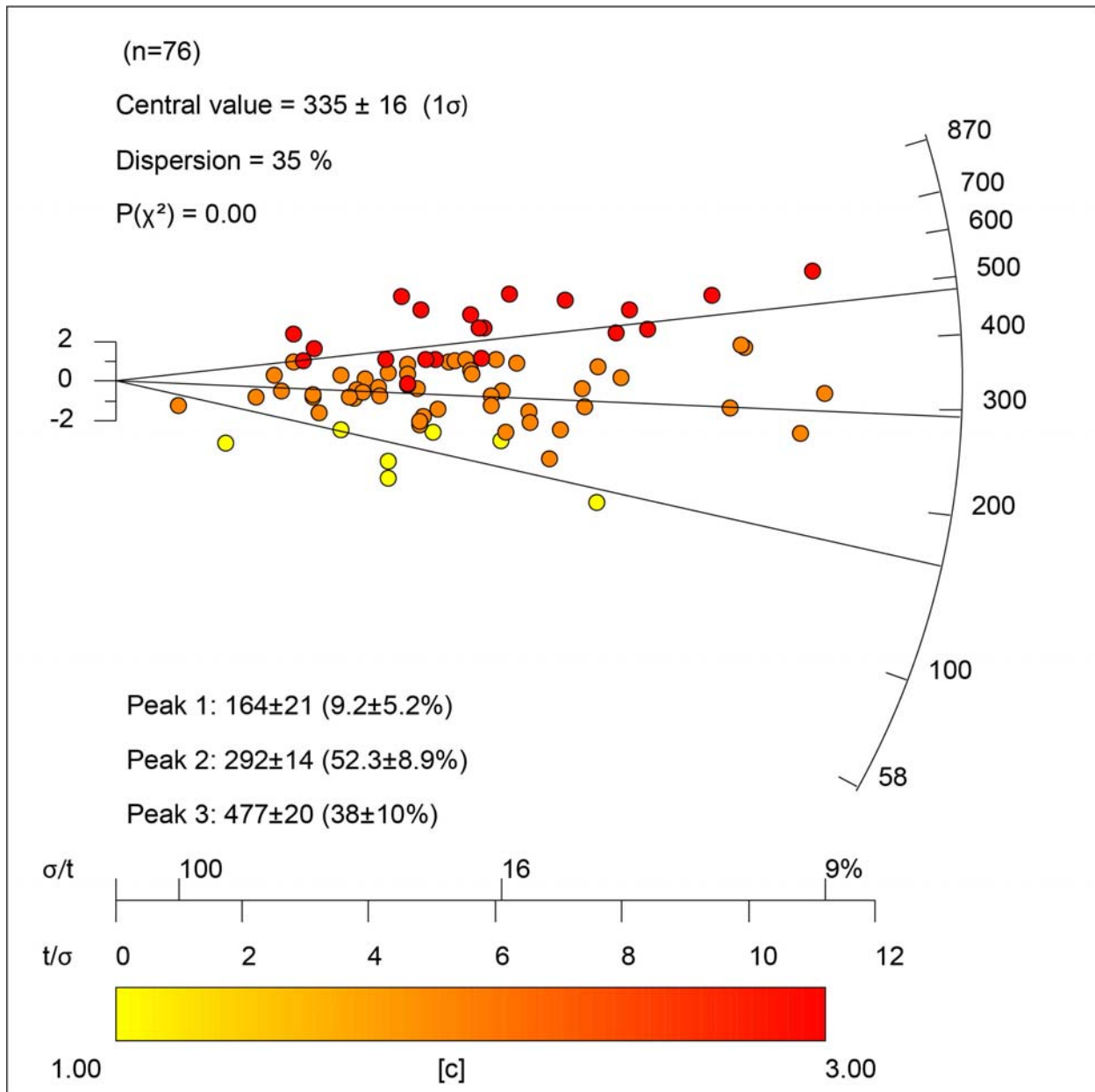


Fig. S4. Radial plot of the apatite fission track data for JP019 using RadialPlotter (Vermeesch, 2009). Fission track dates and their associated error are plotted as a function of the degree of rotation along, and distance from, the curved axis. Pooled and central ages from two of the three proposed kinetic populations (Table 1, S1) are within error of the peak ages predicted from the radial plot, whereas the third (peak 3 = 477 ± 20 Ma; pooled age = 520.1 ± 20.8 Ma) is slightly outside of analytical error.

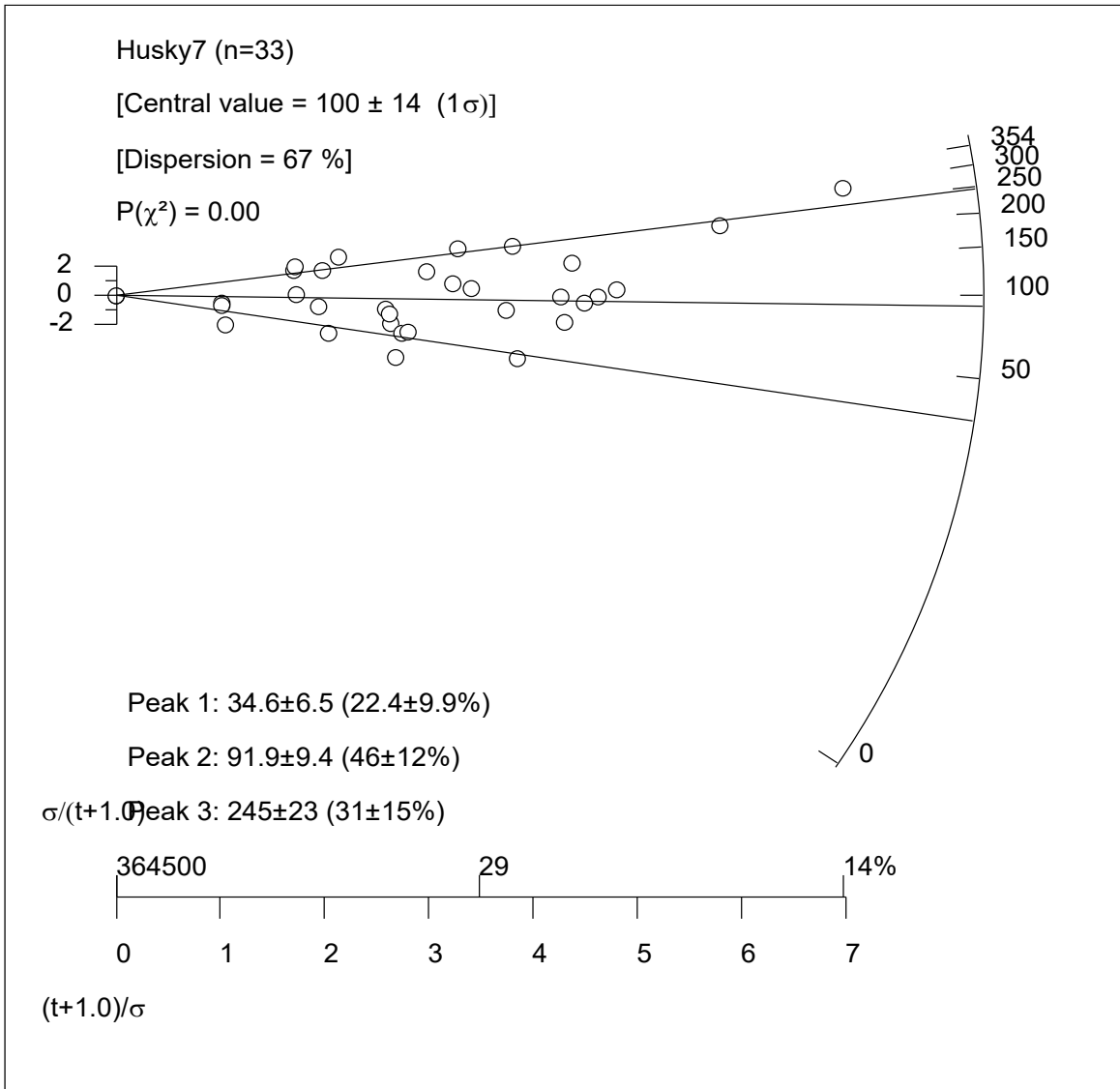


Fig. S5. Radial plot of the apatite fission track data for Husky7 using RadialPlotter (Vermeesch, 2009). Fission track dates and their associated error are plotted as a function of the degree of rotation along, and distance from, the curved axis. Pooled ages of the three proposed kinetic populations (Table 1, S1) are within error of the peak ages predicted from the radial plot.

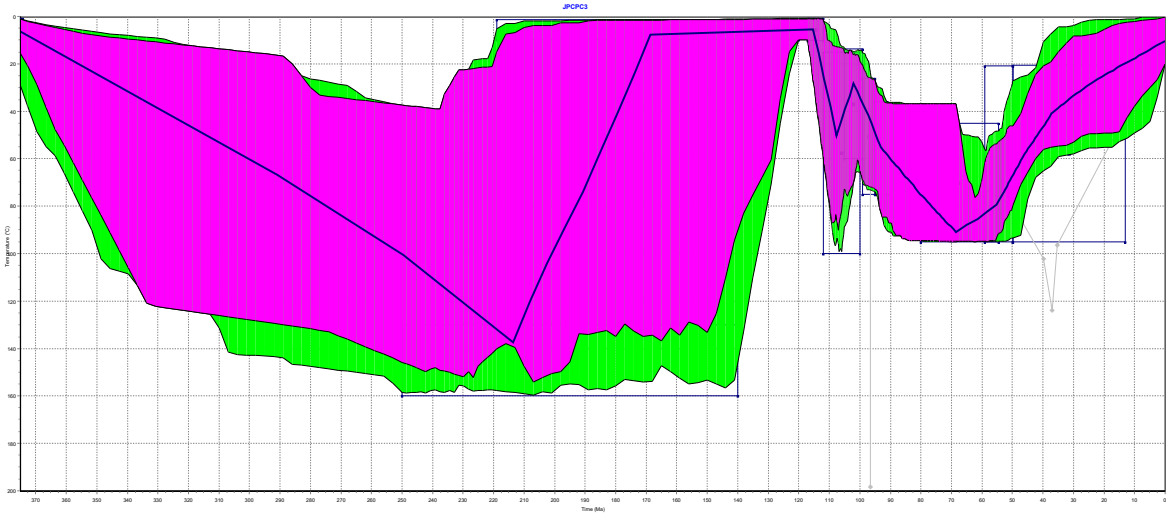


Fig. S6. Inverse thermal model for AHe dates from the Imperial Formation sample JPCPC3. ‘Good fit’ thermal histories are summarized by the purple envelope, whereas ‘acceptable’ solutions are highlighted in green. The blue line represents the weighted mean of all good and acceptable time-temperature solutions. X-axis is from 375 – 0 Ma, and Y-axis is from 0 – 200 °C. The Albian to present thermal history is expanded in Figure S12.

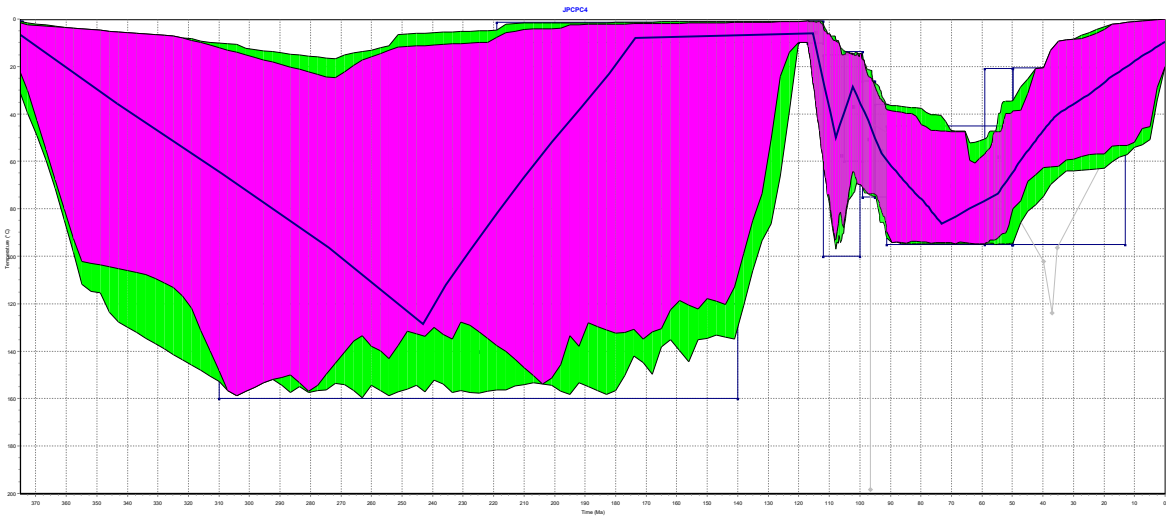


Fig. S7. Inverse thermal model for AHe dates from the Imperial Formation sample JPCPC4. ‘Good fit’ thermal histories are summarized by the purple envelope, whereas ‘acceptable’ solutions are highlighted in green. The blue line represents the weighted mean of all good and acceptable time-temperature solutions. X-axis is from 375 – 0 Ma, and Y-axis is from 0 – 200 °C. The Albian to present thermal history is expanded in Figure S12.



Fig. S8. Inverse thermal model for AHe dates from the Imperial Formation sample 10FNA066. ‘Good fit’ thermal histories are summarized by the purple envelope, whereas ‘acceptable’ solutions are highlighted in green. The blue line represents the weighted mean of all good and acceptable time-temperature solutions. X-axis is from 375 – 0 Ma, and Y-axis is from 0 – 200 °C. The Albian to present thermal history is expanded in Figure S12.

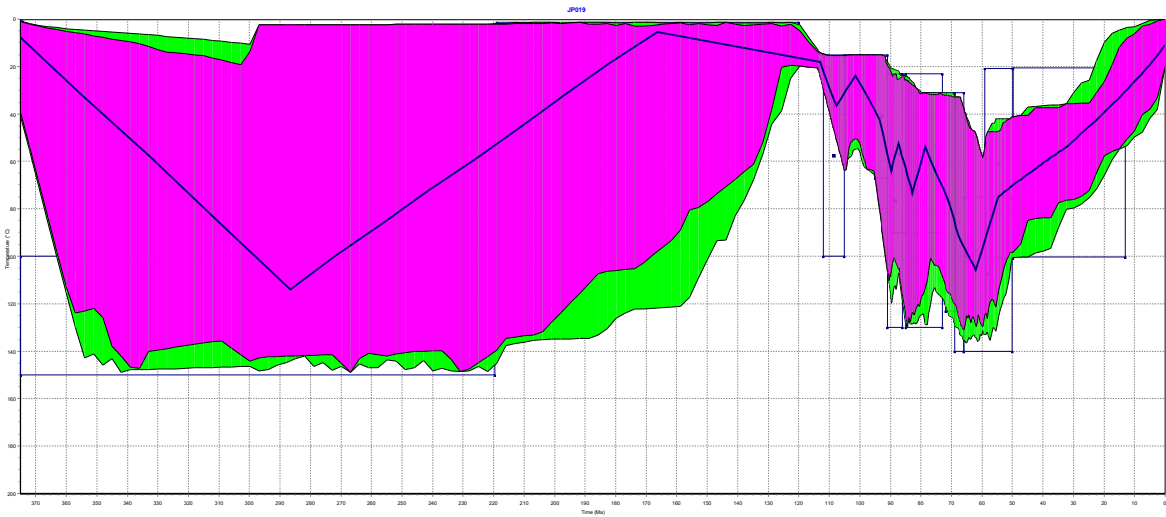


Fig. S9. Inverse thermal model for AHe dates from the Imperial Formation sample JP019. ‘Good fit’ thermal histories are summarized by the purple envelope, whereas ‘acceptable’ solutions are highlighted in green. The blue line represents the weighted mean of all good and acceptable time-temperature solutions. X-axis is from 375 – 0 Ma, and Y-axis is from 0 – 200 °C. The Albian to present thermal history is expanded in Figure S12.



Fig. S10. Inverse thermal model for AHe dates from the Imperial Formation sample 10FNARL008. ‘Good fit’ thermal histories are summarized by the purple envelope, whereas ‘acceptable’ solutions are highlighted in green. The blue line represents the weighted mean of all good and acceptable time-temperature solutions. X-axis is from 375 – 0 Ma, and Y-axis is from 0 – 200 °C. The Albian to present thermal history is expanded in Figure S12.



Fig. S11. Inverse thermal model for AHe dates from the Imperial Formation sample Husky7. ‘Good fit’ thermal histories are summarized by the purple envelope, whereas ‘acceptable’ solutions are highlighted in green. The blue line represents the weighted mean of all good and acceptable time-temperature solutions. X-axis is from 375 – 0 Ma, and Y-axis is from 0 – 200 °C. The Albian to present thermal history is expanded in Figure S12.

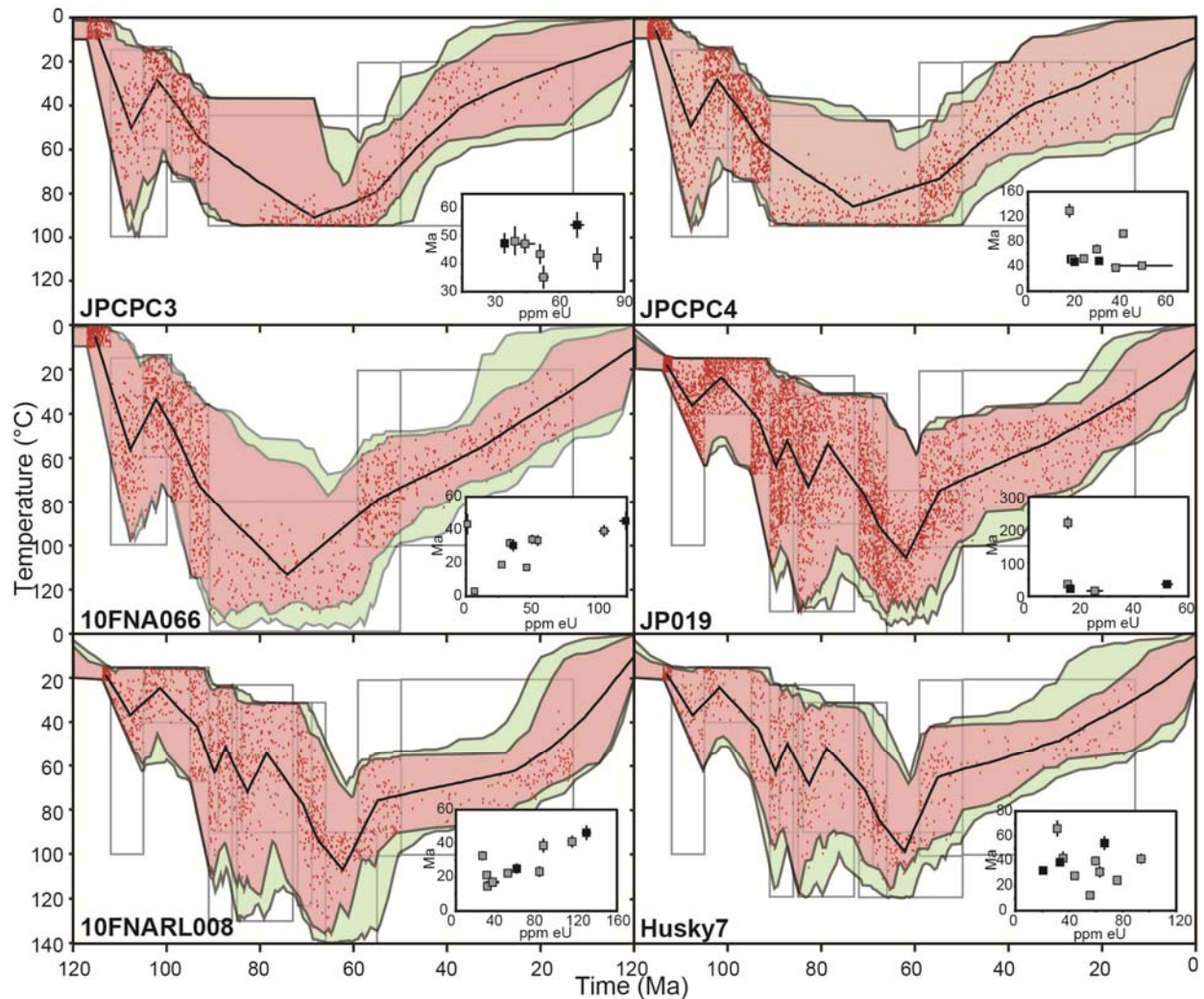


Fig. S12. Inverse thermal history model incorporating AHe data created using HeFTy (Ketcham, 2005). Light green and pink envelopes indicate the realm of T-t solutions for acceptable and good paths, respectively. Red dots indicate the inflection points of good T-t paths. Gray outlined rectangles represent independent temperature-time constraints based on preserved stratigraphic section, unconformities, plausible geothermal gradients, and the range of maximum temperatures as indicated by AFT modeling (**Figure 5, 6**). The black curve indicates the weighted mean T-t path of all acceptable and good solutions. Inset graph shows AHe dates, modified from Figure 4 to account for variable geometries and broken grains. AHe grains in black were incorporated into the inverse model. Although these figures only display the modeled Cretaceous thermal history, expanded models (Devonian to present) are available in the supporting information, as is a table that summarizes age and thickness of Cretaceous stratigraphy incorporated into the models as t-T constraints.